Facile and eco-friendly approach to produce confined metal cluster catalysts

Penghui Yan[a, b], Shibo Xi[c], Hong Peng[b], David R. G. Mitchell[d], Luke Harvey[a], Matthew Drewery[a], Eric M. Kennedy[a], Zhonghua Zhu[b], Gopinathan Sankar[e], Michael Stockenhuber[a*]

[a] *Chemical Engineering, School of Engineering, University of Newcastle, Callaghan, NSW, 2308, Australia.*

[b] *School of Chemical Engineering, University of Queensland, St Lucia, QLD, 4072, Australia*

[c] *Institute of Sustainability for Chemicals, Energy and Environment (ISCE2), Agency for Science, Technology and Research (A*STAR), 1 Pesek Road, Jurong Island 627833, Singapore.*

[d] *Electron Microscopy Centre, AIIM Building, Innovation Campus, University of Wollongong, Fairy Meadow, NSW 2519, Australia.*

[e] *Department of Chemistry, University College London, 20 Gordon Street, London WC1H 0AJ, United Kingdom.*

*E-mail: michael.stockenhuber@newcastle.edu.au

ABSTRACT

Zeolite supported metal nanocluster catalysts have attracted significant attention due to their broad application in heterogeneously catalysed reactions. The preparation of highly dispersed metal catalysts commonly involves the use of organic compounds and requires the implementation of complicated procedures, which are neither green nor deployable at the large scale. Herein, we present a novel facile method (vacuum-heating) which employs a specific thermal vacuum processing protocol of catalysts to promote the decomposition of metal precursors. The removal of coordinated H_2O via vacuum-heating restricts the formation of intermediates (metal-bound OH species), resulting in catalysts with a uniform, metal nanocluster distribution. The structure of the intermediate was determined by *in situ* FTIR, temperature-programmed decomposition and XAS measurements. This alternative synthesis method is eco-friendly and cost-effective as the procedure occurs in the absence of organic compounds. It can be widely used for the preparation of catalysts from different metal species (Ni, Fe, Cu, Co, Zn) and precursors and is readily scaled-up.

KEYWORDS: Vacuum-heating, XAS, Metal-bound OH species, Ni cluster, hydrogenation

1. INTRODUCTION

In general, small active metal particle size catalysts exhibit significantly improved catalytic properties compared to larger particle sizes [1-5]. Catalysts formed from isolated atoms of the noble metals (Pt, Ru, Pd) have been shown to exhibit higher activity in hydrogenation [6, 7], hydrodeoxygenation [8] and C-C coupling [9] compared to supported nano-catalysts.

On the other hand, it has been proposed that atomically dispersed metal catalysts exhibit poor H_2 dissociation activity, attributed to weaker bonding compared to clustered metal catalysts and this reduced dissociation activity results in reduced activity for hydrotreating reactions [10]. Strong metal-support interactions were frequently observed over zeolites and Al_2O_3 supported Ni single-atom and cluster catalysts, resulting in an increased rate of electron transfer from metal to support and a decreased hydrogenation activity compared to catalysts with a high number of nanoparticles [11, 12]. For optimum results, the particle size of Ni should be confined to a specific size distribution to maximize the concentration of surface active sites while minimizing the rate of electron transfer from metal to support.

Catalysts with a high concentration of nanoclusters have been successfully prepared by a variety of methods (e.g. deposition-precipitation, encapsulation, atomic layer deposition, mass-selected soft-landing technique) [13-18]. However, most methods are complex and involve the use of organic solvents (e.g. capping agents), which are not considered “green” nor suitable for industrial manufacturing [19-23]. Moreover, the metal loadings achieved often are too low to obtain a satisfactory activity for practical reactions that commonly occur under harsh conditions (e.g. high temperature, high pressure and high weight hourly space velocity/WHSV). Incipient wetness impregnation is frequently used to prepare bifunctional catalysts due to its ease of scale up [24]. Metal aggregation, however, is inevitable via the traditional impregnation methods even at low loading (< 5 wt%), which generates bulk metal particles (>10 nm) [20, 25].

In this paper, we present a novel, efficient, simple and environmentally friendly modified incipient wetness impregnation approach that allows the preparation of highly-dispersed Ni clusters and smaller nanoparticles (0~3 nm) with high metal loadings (~10 wt%, Table S1). It achieves this in the absence of organic solvent by very carefully heat treating samples under vacuum. TiO_2, SiO_2 and Beta zeolite (BEA) were chosen as supports due to their thermally stability, and because they are widely used in hydrotreating reactions [26-28]. We show that the decomposition of metal precursors and the removal of surface hydroxy groups was promoted by vacuum-heating the catalyst at 260 °C. Further, it was found that the removal of hydroxy groups, which were bound to Ni species, restricted the aggregation of NiO nanoclusters (< 2 nm) to form bulk nanoparticles (> 7 nm) at higher calcination temperatures

(350-500 °C). The detailed catalyst preparation procedure, catalyst characterization and catalytic testing information are described in the supplementary Information.

2. RESULTS and DISCUSSION

2.1. Catalyst Characterization

Characterization of samples by powder X-ray diffraction (PXRD, Figure 1a, S1) showed a significant decrease in reflections corresponding to NiO (JCPD no. 04-0835) for Ni/BEA-vac-500, Ni/TiO_2-vac-500, and Ni/SiO_2-vac-500 compared to the equivalent specimens calcined in air, suggesting vacuum heating promoted the formation of smaller Ni species. The XRD patterns of supports are provided in Figure S2. The TEM images, particle size distribution and EDS maps of Ni/BEA and Ni/TiO_2 (Figure S3-4) also indicate the vacuum heated samples possess a narrower metal particle size distribution (range = 0-9 nm) and a smaller mean metal particle size (d_{Ni}=3.9-4.3 nm) compared to air calcination samples.

The untreated Ni/BEA sample was heated to 260 °C and 350 °C to further investigate the influence of vacuum and air treatments on the state of nickel (e.g. structure and particle size). The Ni/BEA-thin-vac-260 and Ni/BEA-thin-vac-500 samples were prepared by vacuum heating the uncalcined Ni/BEA thin pellets (thickness of 0.013 cm) to 260 °C and 500 °C, respectively, which aims to investigate the influence of pellet thickness and heating temperature on the structure of intermediate and metal particle size. As shown in Figure 1b, a reduced intensity of NiO reflections was observed over Ni/BEA-vac-260 and Ni/BEA-vac-thin-260, indicating the $Ni(NO_3)_2{\cdot}6H_2O$ was decomposed to smaller NiO particles at 260 °C by heating the uncalcined Ni samples in vacuum. In contrast, these NiO diffraction peaks were absent over Ni/BEA-air-260 and Ni/BEA-air-thin-260, with a small peak detected at 12.8 °. This could be attributed to the nickel oxide hydroxide [29], suggesting the $Ni(NO_3)_2{\cdot}6H_2O$ was decomposed to $NiO_x(OH)_y$ species in air at 260 °C. It is noted that the full width at half maximum (FWHM) of NiO (2 0 0) diffraction peak over Ni/BEA-vac-thin-260 (1.8 °) was larger than that of Ni/BEA-vac-260 (1.0 °), indicating the metal dispersion was further improved by increasing the surface-to-volume ratio.

HAADF-STEM images revealed the small NiO nano-clusters (0~2 nm) and small nanoparticles (2~3 nm) were dispersed on the BEA support over Ni/BEA-thin-air-260 as well as Ni/BEA-thin-vac-260 (Figure 1c-d, Figure S5-6), indicating the NiO and $NiO_x(OH)_y$ species both were present as small particles (~1.7 nm) after heating at 260 °C, in line with XRD analysis. The particle size of Ni/BEA-thin-vac-500 (Figure 1e, Figure S7-8) was similar with that of Ni/BEA-thin-vac-260 (Figure 1d), suggesting the small NiO species were not aggregated to large NiO particles at higher calcination temperature, also supported by XRD analysis.

The high intensity of NiO diffraction peaks over Ni/BEA-air-350 (Figure 1b) indicates $NiO_x(OH)_y$ species underwent agglomeration to bulk NiO nanoparticles when the calcination temperature increased from 260 °C to 350 °C. There were no significant changes observed in the FWHM of NiO (2 0 0) peak of Ni/BEA-vac-350 (1.1 °) and Ni/BEA-vac-500 (1.1 °) compared to Ni/BEA-vac-260 (1.0 °), demonstrating that the small NiO particles formed at 260 °C did not aggregate into large NiO species at higher calcination temperature. Given the high Tamman temperature of NiO (841 °C) [30], 260 °C corresponds to a relatively low temperature, restricting the migration of NiO species. The metal dispersion obtained by chemisorption is shown in Figure 1f. In line with the analysis of XRD and TEM, the vacuum treated catalysts exhibited a remarkably high dispersion compared to air calcination catalysts. In addition, it is noted the Ni/TiO_2-vac-120-air-500, which was degassed before heat treatment to 120 °C, followed by heating up to 500 °C in air, displayed a significantly lower dispersion compared to Ni/TiO_2-air-120-vac-500 and Ni/TiO_2-vac-500, indicating the application of vacuum below 120 °C did not improve the metal dispersion. In contrast, Ni/TiO_2-air-260-vac-500 and Ni/TiO_2-vac-260-air-500 samples exhibited a high dispersion, as did Ni/TiO_2-vac-500, indicating the application of vacuum around 260 °C promoted metal dispersion.

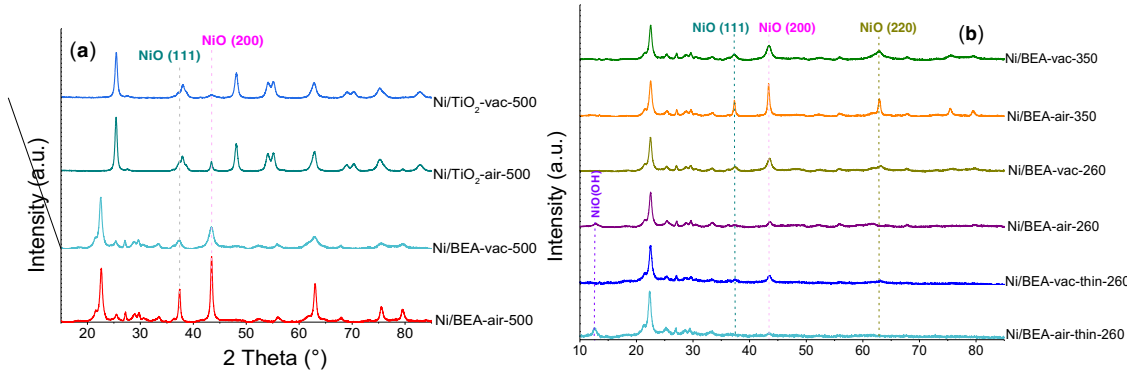

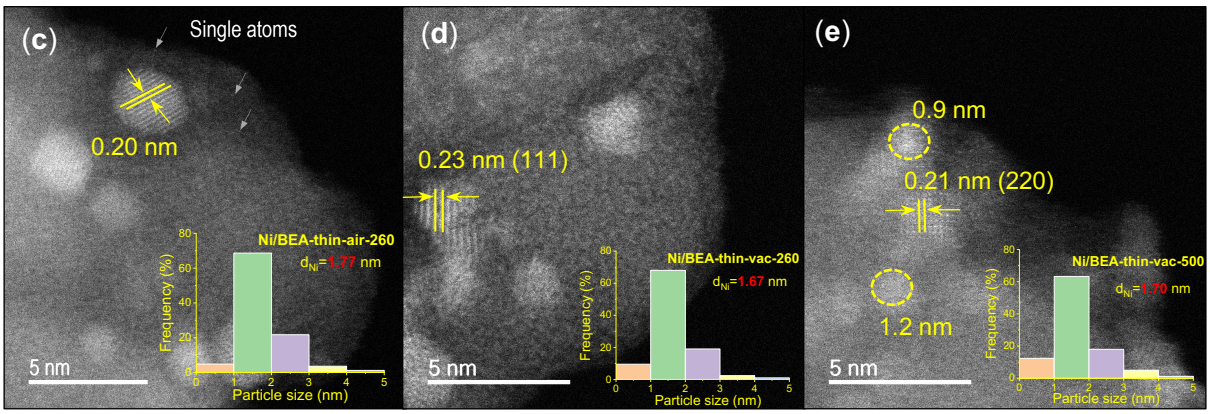

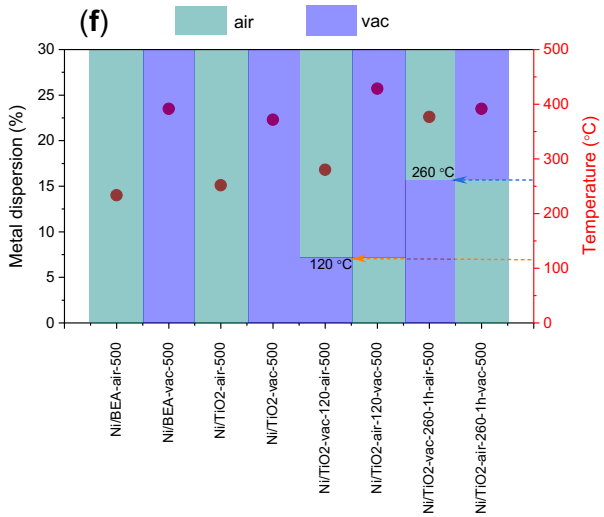

Figure 1. (a, b) XRD patterns of calcined samples; HAADF-STEM images of (c) Ni/BEA-thin-air-260, (d) Ni/BEA-thin-vac-260 and (e) Ni/BEA-thin-vac-500; (f) metal dispersion of catalysts with various calcination models.

H_2-temperature-programmed reduction was carried out to investigate the reducibility of BEA supported Ni catalysts with varied metal size, with profiles shown in Figure 2a. A significantly higher reduction peak around 425 °C was detected over Ni/BEA-air-500, attributed to the reduction of large Ni nanoparticles weakly interacting with support [31, 32]. The higher temperature peak centred around 510-550 °C was attributed to the reduction of smaller Ni nanoparticles and clusters, which possess a strong interaction with BEA zeolite [11]. The Ni/BEA-thin-vac-500 exhibited the highest peak area around 510 °C, followed by Ni/BEA-vac-500 and Ni/BEA-air-500, indicating a higher concentration of smaller NiO particles present in the vacuum treated samples. In addition, a small but distinct peak at 587 °C was observed over Ni/BEA-thin-vac-500, which could be attributed to the reduction of isolated Ni cations and/or clusters situated in the zeolite pores [32]. The interaction of Ni nanoparticle with BEA was weak and the interaction of Ni single atoms with BEA was strong. In contrast, the Ni/TiO_2-vac-500 with smaller Ni particles exhibited the main reduction peak at 378 °C where the highest reduction peak of bigger NiO nanoparticles over Ni/TiO_2-air-500 was at 488 °C (Figure S9). The different reduction temperature of small Ni species over Ni/BEA and Ni/TiO_2 indicates the strength of the interaction between Ni species and support is not only related to the size of Ni particles, but also linked to the nature of support.

The surface oxidation state of Ni in the prepared catalysts was investigated by X-ray photoelectron spectroscopy (XPS) with the fitted spectra and second derivative spectra displayed in Figure 2b and Figure S10. Two main peaks centred around 856 eV and 858 eV were observed, assigned to the Ni $2p_{3/2}$ of NiO and $Ni(OH)_x$, respectively [33, 34]. It is reported that the $Ni(OH)_x$ species was formed by surface layer of NiO interacting with moisture in the

air [35-37]. All vacuum-heating samples show higher peak area ratios of $Ni(OH)_x$ $2p_{3/2}$ to NiO $2p_{3/2}$ compared to the air-calcination samples (Table S2), suggesting a higher amount of surface Ni species over the vacuum-heating samples. This is also confirmed by the highest surface atomic ratio of Ni to Si (surface $r_{Ni/Si}$) over Ni/BEA-thin-vac-500 (0.282), followed by Ni/BEA-vac-500 (0.165) and Ni/BEA-air-500 (0.083). The Ni/BEA-thin-vac-500 shows the highest surface $r_{Ni/Si}$ and larger peak ratio of $Ni(OH)_x$ $2p_{3/2}$ to NiO $2p_{3/2}$, indicating the metal dispersion was further improved by decreasing the thickness of the specimen, in line with XRD and HAADF-STEM analysis (Figure 1b, e). While a large $Ni(OH)_x$ peak was observed over the vacuum-heating samples in XPS spectra, the diffraction peaks of $Ni(OH)_x$ [38, 39] were absent in the XRD patterns, which could be ascribed to the small size of $Ni(OH)_x$ species that were formed in the surface layer beyond the detection of XRD. In addition, a small peak at 860.2 eV with satellite peak at 866.6 eV was observed over the Ni/BEA-thin-vac-500, which could be ascribed to the isolated Ni cations located in the micropores strongly interacting with BEA support and charge-compensating the framework.

The effect of vacuum pressure and support type on the metal dispersion was studied by XPS. The surface Ni/Si atomic ratio was not significantly increased by lowering the vacuum pressure from 10^{-2} (Figure S11) to 10^{-7} mbar (Figure 2b), indicating the metal dispersion was not further improved by lowing the vacuum pressure during the calcination. In addition, an increased surface Ni concentration and peak area of $Ni(OH)_x$ was observed over vacuum-heated Ni/TiO_2 and Ni/SiO_2 samples compared to air calcined samples (Table S2, Figure S12), suggesting the vacuum-heating method can improve the metal dispersion of nickel catalysts over diverse supports.

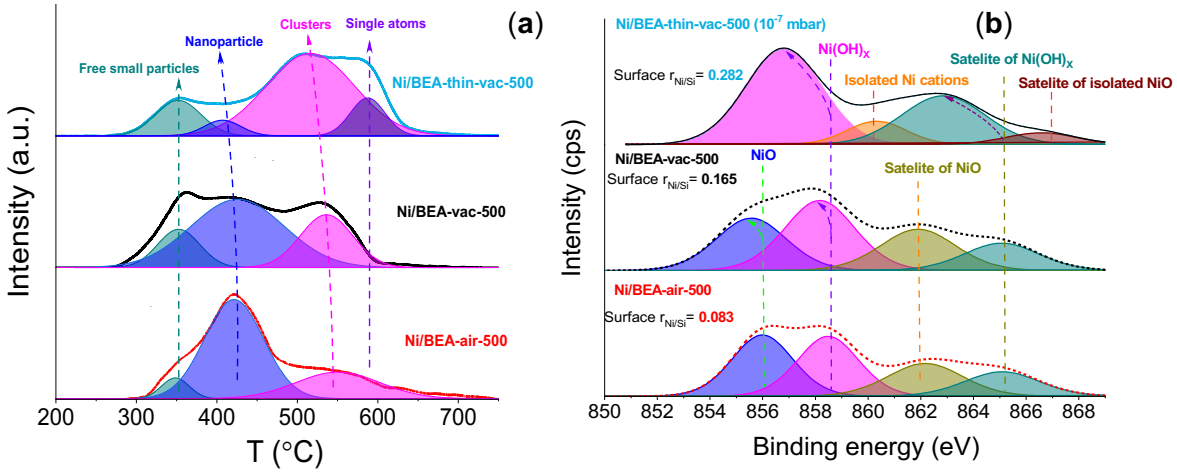

Figure 2. (a) H_2-TPR of Ni/BEA catalysts and (b) XPS of Ni/BEA catalysts.

2.2. Mechanistic Investigation of the Formation of Ni Clusters

Temperature-programmed-decomposition, in situ FTIR and EXAFS experiments were carried out to determine the formation mechanism of Ni clusters during vacuum-heating. Temperature-programmed-decomposition profiles of $Ni(OH)_2$ and $Ni(NO_3)_2{\cdot}6H_2O$ can be seen in Figure 3a, with the desorbed H_2O and NO_2 value displayed in Table S3. The majority of coordinated H_2O (*m/z*=18) was initially removed from $Ni(NO_3)_2{\cdot}6H_2O$ below 200 °C, with 1.9 mmol NO_2 and 0.3 mmol H_2O fully removed around 270 °C. In contrast, the peak maxima of H_2O over $Ni(OH)_2$ was at 236 °C, suggesting the OH groups were strongly bound to Ni species compared to the coordinated water in $Ni(NO_3)_2{\cdot}6H_2O$. The Ni/TiO_2-uncalcined displayed a similar behaviour to $Ni(NO_3)_2{\cdot}6H_2O$, with 2 NO_2 and 0.5 H_2O decomposed around 250 °C (Figure 3b). The small amount of decomposed H_2O above 200 °C over Ni/TiO_2-uncalcined, Ni/BEA-uncalcined and $Ni(NO_3)_2{\cdot}6H_2O$ could be ascribed to the OH groups being strongly bound to Ni species.

The peaks of *m/z*=18 (H_2O) and *m/z*=46 (NO_2) were not observed for Ni/TiO_2-vac-260-1h, indicating that the $Ni(NO_3)_2{\cdot}6H_2O$ was fully decomposed to NiO, H_2O, NO_2 and O_2 at 260 °C under vacuum condition. In contrast, 0.4 units of H_2O was still observed over Ni/TiO_2-air-260-1h, suggesting calcination under air atmosphere below 260 °C was unable to remove the OH groups strongly bound to Ni species.

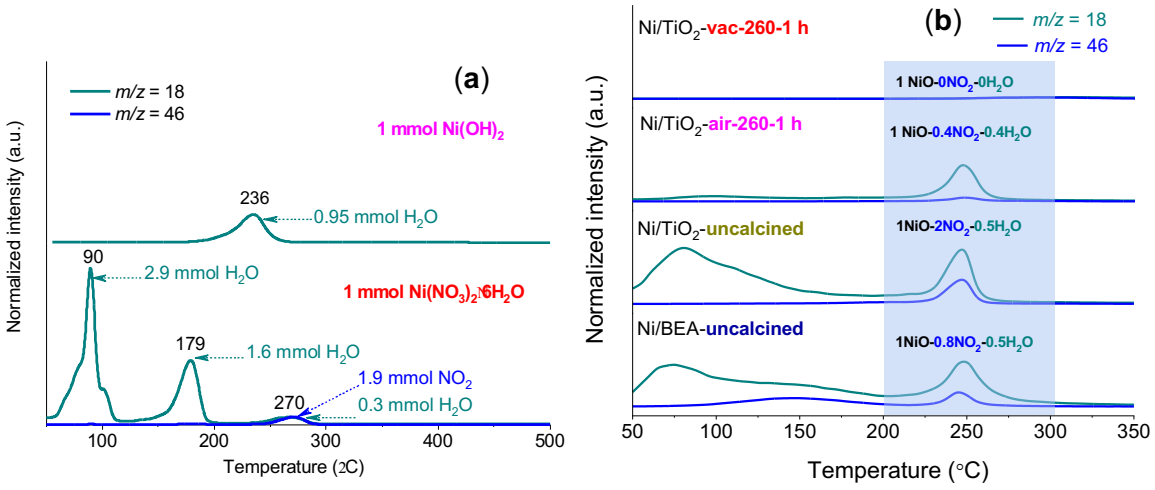

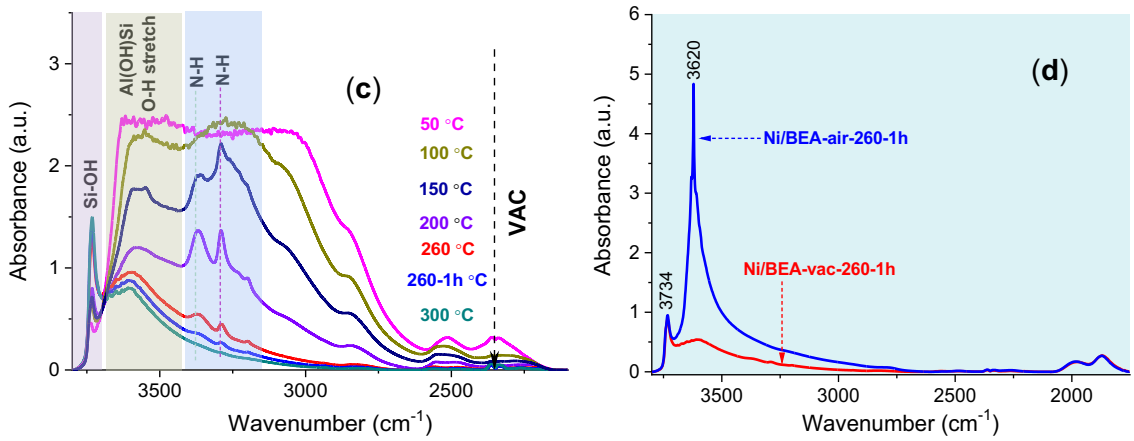

Figure 3. (a) Temperature-programmed-decomposition of $Ni(NO_3)_2{\cdot}6H_2O$ and $Ni(OH)_2$, the signal was detected by mass spectrometry and the intensity was normalized to 1 mmol mass of sample. (b) Temperature-programmed-decomposition profiles of Ni/TiO_2-vac-260-1h, Ni/TiO_2-air-260-1h, Ni/TiO_2-uncalcined and Ni/BEA-uncalcined, the intensity of Ni/TiO_2-vac-260-1h, Ni/TiO_2-air-260-1h, Ni/TiO_2-uncalcined was normalized by 0.1 g of uncalcined Ni/TiO_2. (c) *In situ* FTIR spectra of Ni/BEA-uncalcined, ramp up at 1 °C/min from room temperature to 260 °C, and hold for 1 h then heat up to 300 °C under the pressure of below 10^{-6} mbar. (d) FTIR spectra of Ni/BEA-air-260-1h and Ni/BEA-vac-260-1h at 200 °C under vacuum, the Ni/BEA-air-260-1h and Ni/BEA-vac-260-1h were pre-treated by *in situ* calcination at 260 °C for 1 h under air and vacuum, respectively, ramp up rate 1 °C/min.

FTIR spectra of Ni/BEA with various pre-treatments are exhibited in Figure 3c-d. As shown in Figure 3c, the vibrations located at 3291 cm^{-1} and 3368 cm^{-1} were attributed to the N-H vibration of the NH_4^+ group originating from the NH_4-BEA support (Figure S13). The broad band around 3600 cm^{-1} was assigned to the vibration of OH [40, 41], which was mainly from the coordinated H_2O as the intensity of Al(OH)Si was very low (Figure S13). The intensity of OH vibrations decreased with increasing temperature up to 260 °C, suggesting the decomposition of $Ni(NO_3)_2{\cdot}6H_2O$. At a higher decomposition temperature (300 °C), the intensity of bands in the range of 3000~3700 cm^{-1} was not reduced compared to spectrum at 260 °C, indicating the $Ni(NO_3)_2{\cdot}6H_2O$ was fully decomposed at 260 °C, in line with temperature-programmed-decomposition analysis.

Ni/BEA-air-260-1h exhibited a significantly stronger band around 3622 cm^{-1} compared to Ni/BEA-vac-260-1h (Figure 3d), indicating a high concentration of OH groups which were bound to Ni species. This is in line with the spectrum of $Ni(OH)_2$ (Figure S14), where a broad peak around 3622 cm^{-1} was also detected. The strong OH band in Ni/BEA-air-260-1h catalyst suggests calcination in air below 260 °C was unable to remove the OH groups bound to Ni species.

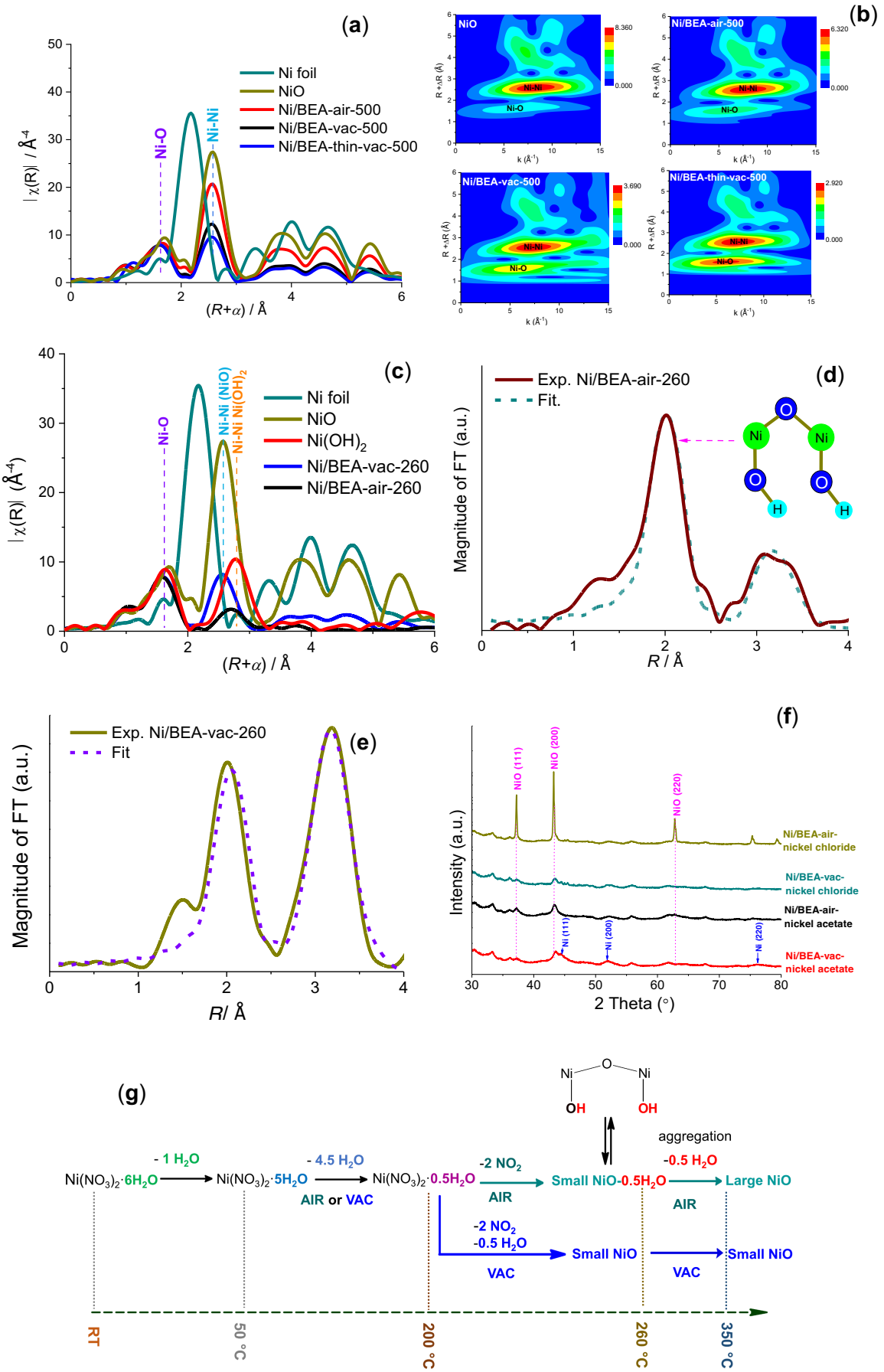
(a)
Ni foil
NiO
Ni/BEA-air-500
Ni/BEA-vac-500
Ni/BEA-thin-vac-500
Ni-O
Ni-Ni
|χ(R)| / Å-4
(R+α) / Å
(b)
NiO
Ni/BEA-air-500
Ni/BEA-vac-500
Ni/BEA-thin-vac-500
Ni-Ni
Ni-O
k (Å-1)
(c)
Ni foil
NiO
Ni(OH)2
Ni/BEA-vac-260
Ni/BEA-air-260
Ni-Ni (NiO)
Ni-Ni Ni(OH)2
|χ(R)| (Å-4)
(d)
Exp. Ni/BEA-air-260
Fit.
Magnitude of FT (a.u.)
R / Å
(e)
Exp. Ni/BEA-vac-260
Fit
Magnitude of FT (a.u.)
R/ Å
(f)
NiO (111)
NiO (200)
NiO (220)
Ni/BEA-air-nickel chloride
Ni/BEA-vac-nickel chloride
Ni/BEA-air-nickel acetate
Ni/BEA-vac-nickel acetate
Intensity (a.u.)
2 Theta (°)
(g)
- 1 H2O
- 4.5 H2O
AIR or VAC
-2 NO2
AIR
aggregation
-0.5 H2O
AIR
-2 NO2
-0.5 H2O
VAC
VAC
Ni(NO3)2·6H2O
Ni(NO3)2·5H2O
Ni(NO3)2·0.5H2O
Small NiO-0.5H2O
Large NiO
Small NiO
Small NiO
OH
OH
RT
50 °C
200 °C
260 °C
350 °C

Figure 4. (a) Fourier transformed of K^3-weighted EXAFS spectra at R space of Ni/BEA-air-500, Ni/BEA-vac-500, Ni/BEA-thin-vac-500, NiO and Ni foil. (b) The wavelet transforms from experimental data for NiO, Ni/BEA-air-500, Ni/BEA-vac-500, and Ni/BEA-thin-vac-500. (c) Fourier transformed of K^3-weighted EXAFS spectra at R space of Ni/BEA-air-260, Ni/BEA-vac-260, $Ni(OH)_2$, NiO and Ni foil. Corresponding EXAFS (d, e) *R* space fitting curves of Ni/BEA-air-260 and Ni/BEA-vac-260. (f) XRD patterns of Ni/BEA catalysts prepared by varied precursors and pre-treatments. (g) Proposed decomposition of $Ni(NO_3)_2{\cdot}6H_2O$ via the air calcination and vacuum heating pathways

To determine the local structure of the Ni species, X-ray absorption near-edge structure (XANES) and extended X-ray absorption fine structure (EXAFS) were acquired for Ni-based catalysts. The Ni K-edge XANES spectra of Ni-based catalysts exhibit spectra similar to NiO standard (Figure S15), indicating the Ni^{2+} is the dominant oxidation state in the prepared Ni samples. In the Fourier-transformed K^3-weighted EXAFS spectra (Figure 4a), two dominant peaks at about 1.60 Å and 2.55 Å are assigned to Ni-O and Ni-Ni scattering paths, respectively. The Ni/BEA-thin-vac-500 exhibited the lowest intensity of Ni-Ni scattering paths, followed by Ni/BEA-vac-500 and Ni/BEA-air-500, suggesting a decreased number of neighbouring Ni atoms over the vacuum-heating samples, in line with the fitted results (Table S4 and Figure S16). In addition, the wavelet transform plot of Ni/BEA-thin-vac-500 exhibited the highest intensity of Ni-O bond (Figure 4b), indicating an increased number of isolated NiO species.

The lower dispersion of Ni/BEA-vac-500 compared to Ni/BEA-thin-vac-500 is attributed to its lower surface area to volume ratio, which results in a high concentration of internal physically adsorbed water and promotes the formation of hydroxy species bound to Ni below 110 °C (Figure S17-18, Table S5). The nickel bound hydroxy species, which were decomposed between 200 and 300 °C, played an important role in metal aggregation. The decreased intensity of Ni-Ni scattering paths was also observed over Ni/TiO_2-vac-500 and Ni/SiO_2-vac-500 compared to the corresponding air-calcination samples (Figure S19).

Based on the structures, literature [35, 42] and fitted values of NiO and $Ni(OH)_2$ standards (Figure S20 and Table S6), the Ni-O distance of NiO (2.08 Å) and $Ni(OH)_2$ (2.07 Å) is almost the same, however, the Ni-Ni distance in $Ni(OH)_2$ (3.12 Å) is significantly higher compared to that of NiO (2.95 Å). Therefore, the position of Ni-Ni scatting path could be used as an indication of the ligands and local structure of the Ni species. The observed position of Ni-Ni scatting paths over Ni/BEA-vac-260 is similar to NiO (Figure 4c), indicating the $Ni(NO_3)_2{\cdot}6H_2O$ was decomposed to NiO under vacuum at 260 °C. In contrast, the Ni-Ni scatting path position of Ni/BEA-air-260 in Figure 4c is between that of NiO and $Ni(OH)_2$, indicating the Ni/BEA-air-260 could be composed of two types of Ni-Ni scatting paths which were provided by the nickel oxide hydroxide species generated via air calcination at 260 °C. The fitted results (Figure 4d-e, Figure S21 and Table S6) confirmed two types of Ni-Ni shells over Ni/BEA-air-260, which is in line with XRD, *in-situ* FTIR and temperature-programmed desorption results. Moreover,

the Ni/BEA-air-260 exhibited similar Ni-O and Ni-Ni coordination number with that of Ni/BEA-vac-260, indicating the bulk NiO particles were not formed over Ni/BEA-air-260 at 260 °C, which agrees with XRD and HAADF-STEM analysis.

Based on the results from temperature-programmed decomposition, *in-situ* FTIR, XPS, XRD, XAS, the mechanism to form large NiO and small NiO particles via air calcination and vacuum heating treatments is proposed in Figure 4g. The $Ni(NO_3)_2{\cdot}6H_2O$ lost 1 unit of coordinated H_2O before 50 °C to form $Ni(NO_3)_2{\cdot}5H_2O$, followed by the decomposition of 4.5 units coordinated H_2O to $Ni(NO_3)_2{\cdot}0.5H_2O$ from 50 °C to 200 °C. At this stage, the OH groups were coordinated to Ni species, thus requiring a high temperature to be decomposed. $Ni(NO_3)_2{\cdot}0.5H_2O$ was fully decomposed to NO_2 O_2, H_2O and Ni clusters when the temperature increased from 200 °C to 260 °C under vacuum (< 10^{-2} mbar). In contrast, when heated in air at 260 °C, only NO_3 was decomposed to NO_2 and O_2, while 0.5 unit H_2O was still bound to Ni^{2+} species. The OH groups bound to Ni species promoted the aggregation of smaller Ni hydroxy species to form bulk NiO nanoparticles when the temperature increased from 260 to 350 °C. The small NiO species formed via vacuum-heating were not agglomerated to larger NiO particles when temperature increased from 260 °C to 500 °C due to its low mobility and high melting point of the oxidic cluster.

2.3. Other Nickel Precursors

Nickel chloride ($NiCl_2$) and nickel acetate tetrahydrate ($Ni(CH_3CO_2)_2{\cdot}4H_2O$) precursors were also used to prepare 9.8 wt% Ni/BEA-$NiCl_2$ and 8.1 wt% Ni/BEA-nickel acetate catalysts by air-calcination and vacuum-heating methods. As displayed in Figure 4f, the intensity of NiO diffraction peaks over Ni/BEA-air-nickel acetate and Ni/BEA-vac-nickel acetate catalysts are both quite low, indicating the presence of a distribution of small NiO particles. Metallic Ni species were detected over Ni/BEA-vac-nickel acetate, attributed to the reduction of NiO via vacuum-heating procedure, in line with XPS analysis (Figure S22-23). In contrast, Ni/BEA-air-nickel chloride shows significantly higher intensity of NiO diffraction peaks than that of Ni/BEA-vac-nickel chloride, indicating larger NiO nanoparticles distribution. Reduced Ni/BEA-air-nickel chloride also displays higher intensity of metallic Ni diffraction peaks compared to that of reduced Ni/BEA-vac-nickel chloride (Figure S24). TEM images and metal particle distribution (Figure S25) indicate the Ni/BEA-vac-nickel acetate has the smallest Ni average particle size (3.3 nm), followed by Ni/BEA-air-nickel acetate (5.4 nm), Ni/BEA-vac-nickel chloride (5.7 nm) and Ni/BEA-air-nickel chloride (7.3 nm), suggesting the vacuum-heating method enhances the nickel dispersion of catalysts over different precursors.

2.4. Other Metals

The Fe, Co, Cu and Zn-based catalysts are widely used in CO_2 conversion [43, 44], reverse water-gas shift [45], Fischer-Tropsch synthesis [46], biomass pyrolysis [47], oil refinery [27], water splitting [48], etc. Therefore, BEA supported Fe (10.9 wt%), Co (10.7 wt%), Cu (11.5 wt%) and Zn (10.3 wt%) catalysts were prepared by air-calcination and vacuum-heating methods to determine whether vacuum-heating can favour the formation of smaller Fe, Co, Cu and Zn particles.

As shown in Figure 5a and Table S7, the vacuum-heating samples show remarkably decreased intensity of CoO (3 1 1), CuO (0 0 2) and Fe_2O_3 (1 0 4) diffraction peaks with larger FWHM values compared to the air-calcination samples, suggesting the vacuum-heating method favoured the formation of smaller CoO, CuO and Fe_2O_3 particles. The diffraction peaks of ZnO were absent over Zn/BEA-vac-500 and Zn/BEA-air-500 samples, in line with literature [49]. The atomic ratios of surface metal (Zn, Co, Cu, Fe) to Si obtained from XPS are summarized in Figure 5b with 2p spectra of metal species displayed in Figure S26. Higher atomic ratios of surface metal to Si are observed over Zn/BEA-vac-500 (0.063), Co/BEA-vac-500 (0.024), Cu/BEA-vac-500 (0.031) and Fe/BEA-vac-500 (0.086) compared to the corresponding Zn/BEA-air-500 (0.046), Co/BEA-air-500 (0.012), Cu/BEA-air-500 (0.017) and Fe/BEA-air-500 (0.037) samples, indicating higher concentration of surface metal species and improved metal dispersion were obtained over the vacuum-heating samples, in agreement with XRD analysis, TEM images and particle size distributions (as shown in Figure S27). These results demonstrate the vacuum-heating method is an effective strategy to prepare diverse metal (e.g. Ni, Fe, Co, Cu, and Zn) catalysts with smaller metal particle sizes.

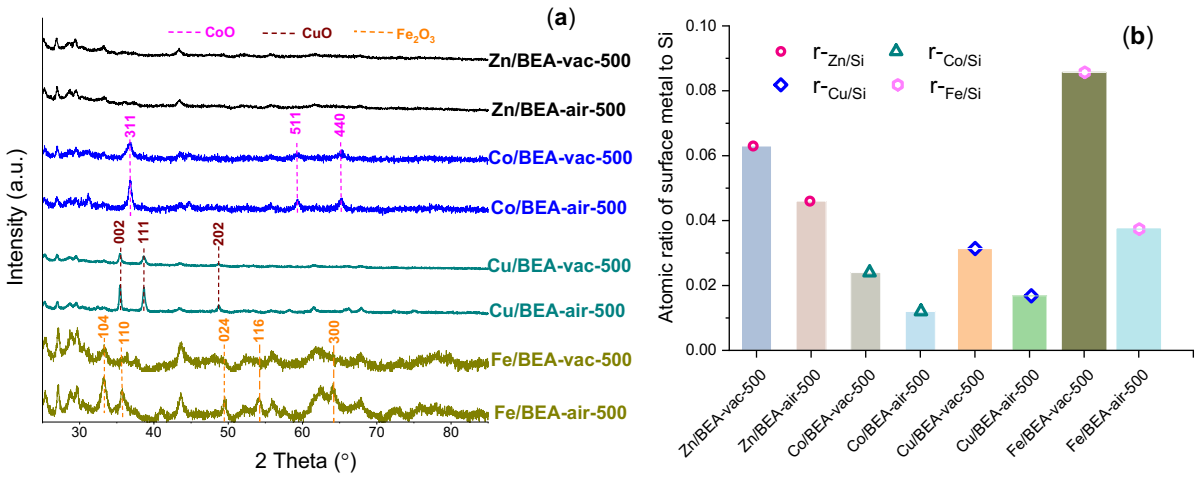

Figure 5. (a) XRD patterns of calcined BEA supported Zn, Co, Cu and Fe samples; (b) atomic ratios of surface metal (Zn, Co, Cu, Fe) to Si over varied catalysts.

2.5. Hydrogenation Performance

The hydrogenation of aromatic compounds is an important reaction for the production of clean and high-quality fuels [50, 51]. The catalytic activities of reduced Ni/BEA catalysts were examined by toluene hydrogenation with the properties characterized by XRD and H_2-TPD. As shown in Figure 6a, the diffraction peaks of metallic Ni (44.6 ° and 52.0 °) were observed over the pre-reduced catalysts, suggesting the NiO particles were reduced to Ni at the reduction temperature of 500 °C. The metal state of reduced Ni/BEA-vac-thin-nickel nitrate was further investigated by a modified H_2-TPR experiment with the reduction temperature held at 500 °C for 2 h (as shown in Figure S28). 98.9% of NiO species was reduced to metallic Ni by H_2 in the temperature range of ≤ 500 °C, indicating the pre-treatment before the reaction can almost fully reduce the NiO nanoparticles as well as clusters to active metallic Ni species. H_2-TPD experiments were performed to investigate the H_2 adsorption/desorption activity of reduced Ni/BEA catalysts with varied metal dispersion and particle size, with profiles exhibited in Figure 6b. The catalysts are mainly composed of low-temperature (low-T < 280 °C) desorbed H_2 and high-temperature (high-T > 280 °C) desorbed H_2. The low-T desorbed H_2 could be ascribed to hydrogen species weakly chemisorbed on the surface of small Ni species [52-54]. The high-T desorbed H_2 can be assigned to the layer of chemisorbed hydrogen between the Ni particles and support or remote from the Ni clusters [53, 55]. As summarized in Table S8, the Ni/BEA-vac-nickel acetate shows the highest peak area of high-T desorbed H_2 (2.94 a.u.), followed by Ni/BEA-vac-nickel nitrate (2.86 a.u.), Ni/BEA-air-nickel acetate (2.07 a.u.), Ni/BEA-vac-thin-nickel nitrate (1.97 a.u.), and Ni/BEA-air-nickel nitrate (1.50 a.u.). The Ni/BEA-vac-thin-nickel nitrate exhibits a lower amount of high-T desorbed H_2 but higher concentration of low-T desorbed H_2, which could be ascribed to its higher concentration of surface Ni clusters strongly interacting with support and weakly chemisorbing the H species on the metal surface.

A high weight hourly space velocity (WHSV=2.8 min^{-1}) was employed for toluene hydrogenation in order to obtain an intrinsic reaction rate in a period of reaction time with the results presented in Figure 6c and Figure S29. The Ni/BEA-vac-nickel acetate shows the highest cycloalkanes formation rate ($3.75 \times 10^{-3} \cdot mol \cdot min^{-1} \cdot g^{-1}$) in the reaction time of 120-300 min, followed by Ni/BEA-vac-nickel nitrate ($3.49 \times 10^{-3} \cdot mol \cdot min^{-1} \cdot g^{-1}$), Ni/BEA-air-nickel acetate ($2.65 \times 10^{-3} \cdot mol \cdot min^{-1} \cdot g^{-1}$), and Ni/BEA-air-nickel nitrate ($2.07 \times 10^{-3} \cdot mol \cdot min^{-1} \cdot g^{-1}$), suggesting the vacuum-heating catalysts have a higher hydrogenation activity compared to air-calcination catalysts, which could be attributed to their improved metal dispersion. In addition, it is noted there is a slight decrease in the cycloalkanes formation rate at the beginning of the reaction, indicating a decrease in the number of active sites, which was also reported by other studies [56, 57]. A high WHSV was used in this study with all accessible active sites saturated by toluene, showing a high initial reaction rate. The metal sites in the small micropores could be

inaccessible for the reactants with time-on-stream due to the diffusional limitation of toluene (critical size of 0.67 nm) [58], leading to a small decrease in the reaction rate.

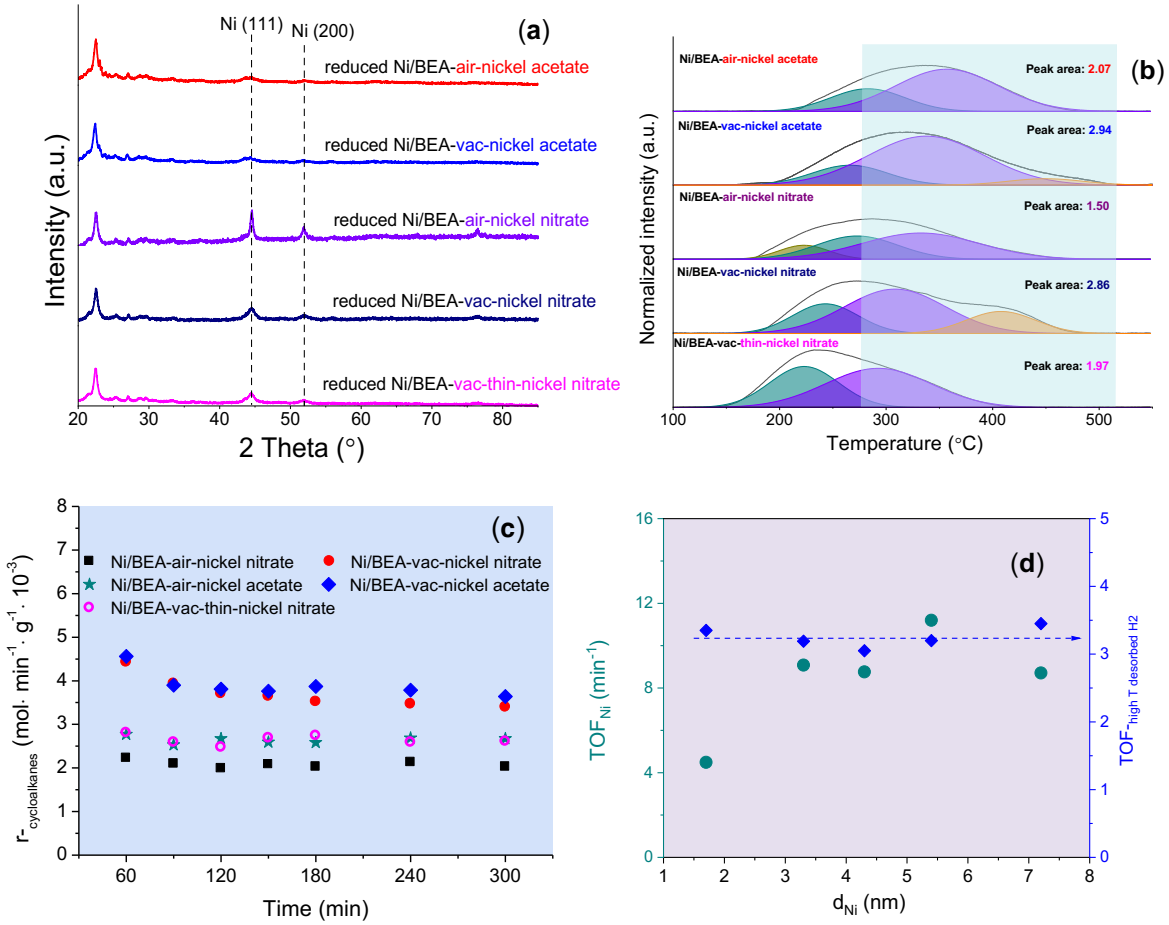

Figure 6. (a) XRD patterns of pre-reduced Ni/BEA catalysts; (b) H_2-TPD profiles of reduced Ni/BEA catalysts; (c) cycloalkanes (methylcyclohexane, dimethyl-cyclopentane, ethyl-cyclopentane) formation rate with time-on-stream in hydrogenation of toluene over Ni/BEA catalysts, reaction conditions: WHSV=2.8 min^{-1}, catalyst mass=50 mg, P_{H2} =500 psi, H_2 flow rate=120 mL/min, T= 220 °C; (d) the relationship of mean Ni particle size (d_{Ni}) and normalized cycloalkanes formation rate (TOF) obtained from the reaction time of 120-300 min, TOF_{Ni}: cycloalkanes formation rate based on the mole of surface Ni (metal loading × dispersion), unit: min^{-1}, $TOF\text{-}_{high\ T\ desorbed\ H2}$: cycloalkanes formation rate based on the peak area of high-temperature desorbed H_2, unit: $mol{\cdot}min^{-1}{\cdot}10^{-4}$/a.u.

The normalized reaction rate (TOF_{Ni}-based on the mole of surface Ni) as a function of mean particle size is plotted in Figure 6d. The Ni/BEA-vac-thin-nickel nitrate displays a TOF_{Ni} value of 4.5 min^{-1}, which is remarkably lower than that of Ni/BEA-air-nickel nitrate (8.7 min^{-1}) and Ni/BEA-vac-nickel nitrate (8.8 min^{-1}). The cycloalkanes formation rate was also normalized by the peak area of high-temperature desorbed H_2 ($TOF\text{-}_{high\ T\ desorbed\ H2}$). All catalysts show a close value of $TOF\text{-}_{high\ T\ desorbed\ H2}$, suggesting the high-temperature surface H species plays a pivotal role in the hydrogenation. Based on TEM and XAS analysis, the Ni/BEA-thin-vac-nickel nitrate

(Ni/BEA-thin-vac-500) exhibited the lowest mean metal particle size (1.7 nm, Figure 1e), followed by Ni/BEA-vac-nickel acetate (3.3 nm, Figure S25b), Ni/BEA-vac-nickel nitrate (4.3 nm, Figure S3a), Ni/BEA-air-nickel acetate (5.4 nm, Figure S25a), and Ni/BEA-air-nickel nitrate (7.2 nm, Figure S3b). The Ni nanoclusters and single atoms over the Ni/BEA-vac-thin-nickel nitrate catalyst exhibit a strong interaction with BEA as shown in H_2-TPR (Figure 2a), which allows significant electrons transfer from Ni to support, leading to a decreased concentration of active H species (high-T desorbed H_2) and lower intrinsic hydrogenation rate. The Ni/BEA-vac-nickel acetate and Ni/BEA-vac-nickel nitrate show higher hydrogenation rates compared to other catalysts, which is ascribed to their high concentration of small Ni nanoparticles (3-4 nm), relatively weak metal-support interaction and increased concentration of high-temperature surface H species.

3. CONCLUSIONS

In summary, Ni nanoclusters and smaller nanoparticles supported by BEA or TiO_2 can be prepared by a simple method. The mechanism by which catalysts with a range of particle sizes can be formed was elucidated by the combined analysis of temperature-programmed desorption, XAS, XPS, *in situ* FTIR and HAADF-STEM. The metal-bound OH species, formed by heating the uncalcined Ni samples in air below 260 °C, promoted the aggregation of small nickel species to form larger diameter Ni nanoparticles from 260 to 350 °C. The application of vacuum and heating removes the hydroxyl groups from uncalcined Ni catalysts below 260 °C, reducing the concentration of metal-bound OH species and obtained a uniform metal nanocluster and relatively narrow nanoparticle distribution. We demonstrate that Ni nanoparticles sized 3 to 4 nm over Ni/BEA-vac-500 exhibited a higher hydrogenation activity compared to Ni nanoclusters (< 2 nm) over Ni/BEA-vac-thin-500 and Ni nanoparticle catalysts larger than 4 nm due to their balance of surface metal concentration, relatively weak interaction with support and increased concentration of high-temperature surface H species. This work established a new cost effective pathway for the preparation of highly dispersed Ni, Cu, Co, Fe catalysts.

4. ASSOCIATED CONTENT

Supporting information (SI)

Detailed experimental procedures; detailed catalyst characterization, XRD patterns, TEM and HAADF-STEM images, H_2-TPR analysis, XANES spectra, EXAFS spectra and curve fitting, in situ FTIR spectra, temperature-programmed desorption profiles, and XPS spectra and curve fitting; detailed performance results of toluene hydrogenation.

Acknowledgements

Funding from the Australian Research Council is gratefully acknowledged. Authors thank the Electron Microscope and X-ray Unit of the University of Newcastle for the help in XRD and TEM analysis. The authors appreciate the Centre for Microscopy and Microanalysis and surface analysis laboratory of UQ, UOW, and UNSW for assistance in HAADF-STEM, XPS and XRD data collection. The authors thank the Singapore Synchrotron Light Source for the help in XAS data collection. The authors thanks Mr James Gudgeon and Mrs Kimiya Bolouri from UQ in XRF analysis.

References

[1] Yang, F.; Liu, D.; Zhao, Y.; Wang, H.; Han, J.; Ge, Q.; Zhu, X. Size Dependence of Vapor Phase Hydrodeoxygenation of m-Cresol on Ni/SiO_2 Catalysts. *ACS Catal.* **2018**, *8*, 1672-1682. https://doi.org/10.1021/acscatal.7b04097

[2] Xu, Z.; Xiao, F. S.; Purnell, S. K.; Alexeev, O.; Kawi, S.; Deutsch, S. E.; Gates, B. C. Size-dependent catalytic activity of supported metal clusters. *Nature* **1994**, *372,* 346-348. https://doi.org/10.1038/372346a0

[3] Song, W.; Zhao, C.; Lercher, J. A. Importance of Size and Distribution of Ni Nanoparticles for the Hydrodeoxygenation of Microalgae Oil. *Chem. Eur. J.* **2013**, *19*, 9833-9842. https://doi.org/10.1002/chem.201301005

[4] Bates, J. S.; Bukowski, B. C.; Harris, J. W.; Greeley, J.; Gounder, R. Distinct Catalytic Reactivity of Sn Substituted in Framework Locations and at Defect Grain Boundaries in Sn-Zeolites. *ACS Catal.* **2019**, *9*, 6146-6148. https://doi.org/10.1021/acscatal.9b01123

[5] Kim, K. D.; Wang, Z.; Tao, Y.; Ling, H.; Yuan, Y.; Zhou, C.; Liu, Z.; Gaborieau, M.; Huang, J.; Yu, A. Selective One-Step Aerobic Oxidation of Cyclohexane to ϵ-Caprolactone Mediated by N-Hydroxyphthalimide (NHPI). *ChemCatChem* **2019**, *11*, 4810-4817. https://doi.org/10.1002/cctc.201900282

[6] Vile, G. A stable single-site palladium catalyst for hydrogenations. *Angew. Chem. Int. Ed.* **2015***, 54*, 11265-11269. https://doi.org/10.1002/anie.201505073

[7] He, X.; He, Q.; Deng, Y.; Peng, M.; Chen, H.; Zhang, Y.; Yao, S.; Zhang, M.; Xiao, D.; Ma, D.; Ge, B.; Ji, H. A versatile route to fabricate single atom catalysts with high chemoselectivity and regioselectivity in hydrogenation. *Nat. Commun.* **2019**, *10*, 3663. https://doi.org/10.1038/s41467-019-11619-6

[8] Mondelli, C.; Gozaydin, G.; Yan, N.; Perez-Ramirez, J. Biomass valorisation over metal-based solid catalysts from nanoparticles to single atoms. *Chem Soc. Rev*. **2020**, *49*, 3764. https://doi.org/10.1039/D0CS00130A

[9] Chen, Z.; Vorobyeva, E.; Mitchell, S.; Fako, E.; Ortuno, M. A.; Lopez, N.; Collins, S. M.; Midgley, P. A.; Richard, S.; Vile, G.; Perez-Ramirez, J. A heterogeneous single-atom palladium catalyst surpassing homogeneous systems for Suzuki coupling. *Nat. Nanotech.* **2018**, *13*, 1-6. https://doi.org/10.1038/s41565-018-0167-2
[10] Jian, M.; Liu, J.; Li, W. Hydroxyl improving the activity, selectivity and stability of supported Ni single atoms for selective semi-hydrogenation. *Chem. Sci.* **2021**, *12*, 10290-10298. https://doi.org/10.1039/D1SC03087F
[11] Yan, P.; Kennedy, E.; Stockenhuber, M. Natural zeolite supported Ni catalysts for hydrodeoxygenation of anisole. *Green Chem*. **2021**, *23*, 4673-4684. https://doi.org/10.1039/D0GC04377J
[12] Xin, H.; Liu, Y.; Hu, C.; Lercher, J. A. Electronic impact of Ni_2P nanoparticle size on hydrogenation rates. *J. Catal.* **2021**, *401*, 129-136. https://doi.org/10.1016/j.jcat.2021.07.017
[13] Peng, H.; Dong, T.; Yang, S.; Chen, H.; Yang, Z.; Liu, W.; He, C.; Wu, P.; Tian, J.; Peng, Y.; Chu, X.; Wu, D.; An, T.; Wang, Y.; Dai, S. Intra-crystalline mesoporous zeolite encapsulation derived thermally robust metal nanocatalyst in deep oxidation of light alkanes. *Nat. Commun.* **2022**, *13*, 295. https://doi.org/10.1038/s41467-021-27828-x
[14] Vajda, S.; White, M. G. Catalysis Applications of Size-Selected Cluster Deposition. *ACS Catal*. **2015**, *5*, 7152-7176. https://doi.org/10.1021/acscatal.5b01816
[15] Wang, J.; Li, Z.; Wu, Y.; Li, Y. Fabrication of Single-Atom Catalysts with Precise Structure and High Metal Loading. *Adv. Mater.* **2018**, *30*, 1801649. https://doi.org/10.1002/adma.201801649
[16] Hai, X.; Xi, S.; Mitchell, S.; Harrath, K.; Xu, H.; Aki, D. F.; Kong, D.; Li, J.; Li, Z.; Sun, T.; Yang, H.; Cui, Y.; Su, C.; Zhao, X.; Li, J.; Perez-Ramire, J.; Lu, J. Scalable two-step annealing method for preparing ultra-high-density single-atom catalyst libraries. *Nat. Nanotech.* **2022**, *17*, 174-181. https://doi.org/10.1038/s41565-021-01022-y
[17] Ji, S.; Chen, Y.; Wang, X.; Zhang, Z.; Wang, D.; Li, Y. Chemical Synthesis of Single Atomic Site Catalysts. *Chem. Rev.* **2020**, *120*, 11900-11955. https://doi.org/10.1021/acs.chemrev.9b00818
[18] Nakatsuka, K.; Yoshii, T.; Kuwahara, Y.; Mori, K.; Yamashita, H. Controlled Pyrolysis of Ni-MOF-74 as a Promising Precursor for the Creation of Highly Active Ni Nanocatalysts in Size-Selective Hydrogenation. *Chem. Eur. J.* **2018**, *24*, 898-905. https://doi.org/10.1002/chem.201704341
[19] Sun, X.; Dawson, S. R.; Parmentier, T. E.; Malta, G.; Davies, T. E.; He, Q.; Lu, L.; Morgan, D. J.; Carthey, N.; Johnston, P.; Kondrat, S. A.; Freakley, S. J.; Kiely, C. J.; Hutchings, G. J. Facile synthesis of precious-metal single-site catalysts using organic solvents. *Nat. Chem.* **2020**, *12*, 560-567. https://doi.org/10.1038/s41557-020-0446-z

[20] Yan, P.; Mensah, J.; Adesina, A.; Kennedy, E.; Stockenhuber, M. Highly-dispersed Ni on BEA catalyst prepared by ion-exchange-deposition-precipitation for improved hydrodeoxygenation activity. *Appl. Catal. B. Env.* **2020**, *267*, 118690-118700. https://doi.org/10.1016/j.apcatb.2020.118690
[21] Lu, P.; Yang, Y.; Yao, J.; Wang, M.; Dipazir, S.; Yuan, M.; Zhang, J.; Wang, X.; Xie, Z.; Zhang, G. Facile synthesis of single-nickel-atomic dispersed N-doped carbon framework for efficient electrochemical CO_2 reduction. *Appl. Catal. B: Env.* **2019**, *241*, 113-119. https://doi.org/10.1016/j.apcatb.2018.09.025
[22] Cheng, Y.; Zhao, S.; Johannessen, B.; Veder, J. P.; Saunders, M.; Rowles, M. R.; Cheng, M.; Liu, C.; Chisholm, M. F.; Marco, R. D.; Cheng, H. M.; Yang, S. Z.; Jiang, S. P. Atomically Dispersed Transition Metals on Carbon Nanotubes with Ultrahigh Loading for Selective Electrochemical Carbon Dioxide Reduction. *Adv. Mat.* **2018**, *30*, 1706287. https://doi.org/10.1002/adma.201706287
[23] Liu, W.; Chen, Y.; Qi, H.; Zhang, L.; Yan, W.; Liu, X.; Yang, X.; Miao, S.; Wang, W.; Liu, C.; Wang, A.; Li, J.; Zhang, T. A Durable Nickel Single-Atom Catalyst for Hydrogenation Reactions and Cellulose Valorization under Harsh Conditions. *Angew. Chem.* **2018**, *130*, 7189-7193. https://doi.org/10.1002/ange.201802231
[24] Edwards, J. K.; Freakley, S. J.; Carley, A. F.; Kiely, C. J.; Hutchings, G. J. Strategies for Designing Supported Gold Palladium Bimetallic Catalysts for the Direct Synthesis of Hydrogen Peroxide. *Acc. Chem. Res.* **2014**, *47*, 845-854. https://doi.org/10.1021/ar400177c
[25] Soares, J. M. C.; Morrall, P.; Crossley, A.; Harris, P.; Bowker, M. Catalytic and noncatalytic CO oxidation on Au/TiO_2 catalysts. *J. Catal.* **2003**, *219*, 17-24. https://doi.org/10.1016/S0021-9517(03)00194-5
[26] Macino, M.; Barnes, A. J.; Althahban, S. M.; Qu, R.; Gibson, E. K.; Morgan, D. J.; Freakley, S. J.; Dimitratos, N.; Kiely, C. J.; Gao, X.; Beale, A. M.; Bethell, D.; He, Q.; Sankar, M.; Hutchings, G. J. Tuning of catalytic sites in Pt/TiO_2 catalysts for the chemoselective hydrogenation of 3-nitrostyrene. *Nat. Catal.* **2019**, *2*, 873-881. https://doi.org/10.1038/s41929-019-0334-3
[27] He, J.; Zhao, C.; Lercher, J. A. Ni-Catalyzed Cleavage of Aryl Ethers in the Aqueous Phase. *J. Am. Chem. Soc.* **2012**, *134*, 20768-20775. https://doi.org/10.1021/ja309915e
[28] Ramirez, A.; Gong, X.; Caglayan, M.; Nastase, S. A. F.; Abou-Hamad, E.; Gevers, L.; Cavallo, L.; Chowdhury, A. D.; Gascon, J. Selectivity descriptors for the direct hydrogenation of CO_2 to hydrocarbons during zeolite-mediated bifunctional catalysis. *Nat. Commun.* **2021**, *12*, 5914. https://doi.org/10.1038/s41467-021-26090-5
[29] Malsbury, A. M.; Greaves, C. The Crystallographic and Magnetic Structure of Ni_2O_3H. *J. Solid State Chem.* **1987**, *71*, 418-425. https://doi.org/10.1016/0022-4596(87)90250-7

[30] Argyle, M. D.; Bartholomew, C. H. Heterogeneous Catalyst Deactivation and Regeneration: A Review. *Catalysts* **2015**, *5*, 145-269. https://doi.org/10.3390/catal5010145
[31] Che, M.; Cheng, Z.; Louis, C. Nucleation and Particle Growth Processes Involved in the Preparation of Silica-Supported Nickel Materials by a Two-Step Procedure. *J. Am. Chem. Soc.* **1995**, *117*, 2008-2018. https://doi.org/10.1021/ja00112a014
[32] Maia, A. J.; Louis, B.; Lam, Y. L.; Pereira, M. M. Ni-ZSM-5 catalysts: Detailed characterization of metal sites for proper catalyst design. *J. Catal.* **2010**, *269*, 103-109. https://doi.org/10.1016/j.jcat.2009.10.021
[33] Akri, M.; Zhao, S.; Li, X.; Zang, K.; Lee, A. F.; Isaacs, M. A.; Xi, W.; Gangarajula, Y.; Luo, J.; Ren, Y.; Cui, Y.; Li, L.; Su, Y.; Pan, X.; Wen, W.; Pan, Y.; Wilson, K.; Li, L.; Qiao, B.; Ishii, H.; Liao, Y.; Wang, A.; Wang, X.; Zhao, T. Atomically dispersed nickel as coke-resistant active sites for methane dry reforming. *Nat. Commun.* **2019**, *10*, 5181. https://doi.org/10.1038/s41467-019-12843-w
[34] Weng, C.; Hu, Z.; Chen, C.; Yuan, Z. Catalytic decomposition of ammonia to CO_x-free hydrogen over Ni/ZSM-5 catalysts: A comparative study of the preparation methods. *Appl. Catal. A: Gen.* **2018**, *562*, 49-57. https://doi.org/10.1016/j.apcata.2018.05.038
[35] Peck, M. A.; Langell, M. A. Comparison of Nanoscaled and Bulk NiO Structural and Environmental Characteristics by XRD, XAFS, and XPS. *Chem. Mater.* **2012**, *24*, 4483-4490. https://doi.org/10.1021/cm300739y
[36] Ratcliff, E. L.; Meyer, J.; Steirer, K. X.; Garcia, A.; Berry, J. J.; Ginley, D. S.; Olson, D. C.; Kahn, A.; Armstrong, N. R. Evidence for near-Surface NiOOH Species in Solution-Processed NiOx Selective Interlayer Materials: Impact on Energetics and the Performance of Polymer Bulk Heterojunction Photovoltaics. *Chem. Mater.* **2011**, *23*, 4988-5000. https://doi.org/10.1021/cm202296p
[37] Fingerle, M.; Tengeler, S.; Calvet, W.; Mayer, T.; Jaegermann, W. Water Interaction with Sputter-Deposited Nickel Oxide on n-Si Photoanode: Cryo Photoelectron Spectroscopy on Adsorbed Water in the Frozen Electrolyte Approach. *J. Electrochem. Soc.* **2018**, *165*, H3148-H3153. https://doi.org/10.1149/2.0191804jes
[38] Lee, J. W.; Ahn, T.; Soundararajan, D.; Ko, J. M.; Kim, J. D. Non-aqueous approach to the preparation of reduced graphene oxide/α-$Ni(OH)_2$ hybrid composites and their high capacitance behavior. *Chem. Comm.* **2011**, *47*, 6305-6307. https://doi.org/10.1039/c1cc11566a
[39] Freitas, M. B. J. G. Nickel hydroxide powder for $NiO{\cdot}OH/Ni(OH)_2$ electrodes of the alkaline batteries. *J. Power Sources* **2001**, *93*, 163-173. https://doi.org/10.1016/S0378-7753(00)00570-X

[40] Scatena, L. F.; Brown, M. G.; Richmond, G. L. Water at Hydrophobic Surfaces: Weak Hydrogen Bonding and Strong Orientation Effects. *Science* **2001**, *292*, 908-912. https://doi.org/10.1126/science.1059514
[41] Belhadj, H.; Melchers, S.; Robertson, P. K. J.; Bahnemann, D. W. Pathways of the photocatalytic reaction of acetate in H_2O and D_2O: A combined EPR and ATR-FTIR study. *J. Catal.* **2016**, *344*, 831-840. https://doi.org/10.1016/j.jcat.2016.08.006
[42] Ichiyanagi, Y.; Kondoh, H.; Yokoyama, T.; Okamoto, K.; Nagai, K.; Ohta, T. X-ray absorption fine-structure study on the $Ni(OH)_2$ monolayer nanoclusters. *Chem. Phy. Lett.* **2003**, *379*, 345-350. https://doi.org/10.1016/j.cplett.2003.08.051
[43] Li, Y.; Li, L.; Yu, J. Applications of Zeolites in Sustainable Chemistry. *Chem*, **2017**, *3*, 928-949. https://doi.org/10.1016/j.chempr.2017.10.009
[44] Wei, J.; Ge, Q.; Yao, R.; Wen, Z.; Fang, C.; Guo, L.; Xu, H.; Sun, J. Directly converting CO_2 into a gasoline fuel. *Nature Commun.* **2017**, *8*, 15174. https://doi.org/10.1038/ncomms15174
[45] Vovchok, D.; Zhang, C.; Hwang, S.; Jiao, L.; Zhang, F.; Liu, Z.; Senanayake, S. D. Rodriguez, J. A. Deciphering Dynamic Structural and Mechanistic Complexity in Cu/CeO_2/ZSM-5 Catalysts for the Reverse Water-Gas Shift Reaction. *ACS Catal.* **2020**. *10*, 10216-10228. https://doi.org/10.1021/acscatal.0c01584
[46] Li, J.; He, Y.; Tan, L.; Zhang, P.; Peng, X.; Oruganti, A.; Yang, G.; Abe, H.; Wang, Y.; Tsubaki, N. Integrated tuneable synthesis of liquid fuels via Fischer–Tropsch technology. *Nature Catalysis* **2018**, *1*, 787-793. https://doi.org/10.1038/s41929-018-0144-z
[47] Mullen, C. A.; Boateng, A. A. Production of Aromatic Hydrocarbons via Catalytic Pyrolysis of Biomass over Fe-Modified HZSM-5 Zeolites. *ACS Sustainable. Chem. Eng.* **2015**, *3*, 1623-1631. https://doi.org/10.1021/acssuschemeng.5b00335
[48] Anantharaj, S.; Ede, S. R.; Sakthikumar, K.; Karthick, K.; Mishra, S.; Kundu, S. Recent Trends and Perspectives in Electrochemical Water Splitting with an Emphasis on Sulfide, Selenide, and Phosphide Catalysts of Fe, Co, and Ni: A Review. *ACS Catal.* **2016**, *6*, 8069-8097. https://doi.org/10.1021/acscatal.6b02479
[49] Mehdad, A.; Lobo, R. F. Ethane and ethylene aromatization on zinc-containing zeolites. *Catal. Sci. Technol.* **2017**, *7*, 3562-3572. https://doi.org/10.1039/C7CY00890B
[50] Saeys, M.; Reyniers, M. F.; Thybaut, J. W.; Neurock, M.; Marin, G. B. First-principles based kinetic model for the hydrogenation of toluene. *J. Catal.* **2005**, *236*, 129-138. https://doi.org/10.1016/j.jcat.2005.09.019
[51] Sebakhy, K. O.; Vitale, G.; Pereira-Almao, P. Dispersed Ni-Doped Aegirine Nanocatalysts for the Selective Hydrogenation of Olefinic Molecules. *ACS Appl. Mater. Interfaces* **2018**, *1*, 6269-6280. https://doi.org/10.1021/acsanm.8b01472

[52] Ceyer, S. T. The Unique Chemistry of Hydrogen beneath the Surface: Catalytic Hydrogenation of Hydrocarbons. *Acc. Chem. Res.* **2001**, *34*, 737-744. https://doi.org/10.1021/ar970030f
[53] Ewald, S.; Standl, S.; Hinrichsen, O. Characterization of nickel catalysts with transient methods. *Appl. Catal. A: Gen.* **2018**, *549*, 93-101. https://doi.org/10.1016/j.apcata.2017.09.023
[54] Znak, L.; Zbak, J. Interaction of Hydrogen with Unsupported and Supported Nickel. *Langmuir* **2006**, *22*, 8758-8763. https://doi.org/10.1021/la0605541
[55] Miller, J. T.; Meyers, B. L.; Barr, M. K.; Modica, F. S.; Koningsberger, D. C. Hydrogen Temperature-Programmed Desorptions in Platinum Catalysts: Decomposition and Isotopic Exchange by Spillover Hydrogen of Chemisorbed Ammonia. *J. Catal.* **1996**, *159*, 41-49. https://doi.org/10.1006/jcat.1996.0062
[56] Ferreira Madeira, F.; Vezin, H.; Gnep, N. S.; Magnuox, P.; Maury, S.; Cadran, N. Radical Species Detection and Their Nature Evolution with Catalyst Deactivation in the Ethanol-to-Hydrocarbon Reaction over HZSM-5 Zeolite. *ACS Catal.* **2011**, *1*, 417-424. https://doi.org/10.1021/cs2000686
[57] Wang, S.; Lu, G. Q. M. CO_2 reforming of methane on Ni catalysts: Effects of the support phase and preparation technique. *Appl. Catal. B. Env.* **1998**, *16*, 269-277. https://doi.org/10.1016/S0926-3373(97)00083-0
[58] Choudhary, V. R.; Nayak, V. S.; Choudhary, T. V. Single-Component Sorption/Diffusion of Cyclic Compounds from Their Bulk Liquid Phase in H-ZSM-5 Zeolite. *Ind. Eng. Chem. Res.* **1997**, *36*, 1812. https://doi.org/10.1021/ie960411h

For the Table of Contents use only

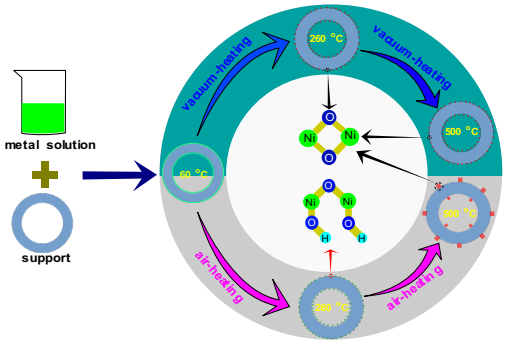

The metal-bound OH species, which promotes the aggregation of metal nanoclusters from 260 to 500°C during air calcination, can be removed below 260 °C by the application of specific thermal vacuum processing, endowing the catalyst with a uniform metal nanocluster and relatively narrow nanoparticle distribution.